NASA

Technical Memorandum 85117

Crustal Deformation, the Earthquake Cycle, and Models of Viscoelastic Flow in the Asthenosphere

Steven C. Cohen and Matthew J. Kramer

OCTOBER 1983

National Aeronautics and
Space Administration

Goddard Space Flight Center
Greenbelt, Maryland 20771

TM 85117

CRUSTAL DEFORMATION, THE EARTHQUAKE CYCLE, AND MODELS OF VISCOELASTIC FLOW IN THE ASTHENOSPHERE

Steven C. Cohen and Matthew J. Kramer

October 1983

GODDARD SPACE FLIGHT CENTER
Greenbelt, Maryland 20771

CRUSTAL DEFORMATION, THE EARTHQUAKE CYCLE, AND MODELS OF VISCOELASTIC FLOW IN THE ASTHENOSPHERE

Steven C. Cohen
Geodynamics Branch
Goddard Space Flight Center
Greenbelt, Maryland 20771 USA
301-344-8826

Matthew J. Kramer
Applied Research Corporation
8201 Corporate Drive
Landover, Maryland 20785 USA

ABSTRACT

The crustal deformation patterns associated with the earthquake cycle can depend strongly on the rheological properties of subcrustal material. Substantial deviations from the simple patterns for a uniformly elastic earth are expected when viscoelastic flow of subcrustal material is considered. The detailed description of the deformation pattern and in particular the surface displacements, displacement rates, strains, and strain rates depend on the structure and geometry of the material near the seismogenic zone. In the past few years various viscoelastic models of crustal deformation have been published. These models differ in their predictions concerning the temporal and spatial patterns of crustal deformation. In some cases these differences are due to varying choices for the physical mechanism under study. In other cases, however, the differences are the result of the details of the mathematical treatment or the choice of model parameters. We seek to resolve the origin of some of these differences by analyzing several different linear viscoelastic models with a common finite element computational technique. The models involve strike-slip faulting and include a thin channel asthenosphere model, a model with a varying

thickness lithosphere, and a model with a viscoelastic inclusion below the brittle slip plane. The calculations reveal that the surface deformation pattern is most sensitive to the rheology of the material that lies below the slip plane in a volume whose extent is a few times the fault depth. If this material is viscoelastic, the surface deformation pattern resembles that of an elastic layer lying over a viscoelastic half-space. When the thickness or breadth of the viscoelastic material is less than a few times the fault depth, then the surface deformation pattern is altered and geodetic measurements are potentially useful for studying the details of subsurface geometry and structure. Distinguishing among the various models is best accomplished by making geodetic measurements not only near the fault but out to distances equal to several times the fault depth. This is where the model differences are greatest; these differences will be most readily detected shortly after an earthquake when viscoelastic effects are most pronounced. For a thin channel asthenosphere model we have found that the predicted displacements are less than those for a half-space asthenosphere. This result is contrary to recently published results based on analytical approximations. The deficiencies of the latter work result from ignoring material below the asthenosphere and in using thickness averaged deformation parameters. Athough the displacements predicted for a thin channel asthenosphere are less than those for a half-space asthenosphere, the postseismic strain rates at intermediate distances from the fault are greater (in an absolute value sense) in the former model.

CRUSTAL DEFORMATION, THE EARTHQUAKE CYCLE, AND MODELS OF VISCOELASTIC FLOW IN THE ASTHENOSPHERE

INTRODUCTION

There are many reasons for the current interest in the development of models of the crustal deformation in active seismic zones. Obviously a thorough understanding of the deformations that develop prior to an earthquake would contribute greatly to predicting a forthcoming event and mitigating the hazards associated with it. The analysis of the deformations that accompany the earthquake provide very basic information on the rupture process, the size of the event, and the state of stress in the lithosphere. Postseismic deformation has been used to study relaxation processes within the asthenosphere and the coupling between surface slip and aseismic creep at depth.

The models that have been developed to account for the crustal deformation of the earthquake cycle fall into two broad catagories, the first involving aseismic slip and the second viscoelastic flow. The purpose of this paper is to analyze in some detail various viscoelastic models of crustal deformation. Our objectives are three-fold. First we want to elucidate which model parameters are likely to be determinable from present or future geodetic measurements. Second we want to compare various models to determine whether the different predictions of alternative models arise from different physical assumptions or different mathematical treatments. Finally we want to determine the range of conditions over which substantial viscoelastic effects are likely to be present. We are primarily interested in the effects of either vertical or lateral confinement of the low

viscosity flow in either the asthenosphere or an intracrustal decoupling layer separating upper and lower elastic lithosphere layers. Models that focus of these problems have either horizontal or lateral variations in viscosity. All of the models that we have investigated use linear viscoelastic rheologies and all are applied to strike-slip faults.

The first of the models relevant to the present study was developed by Savage and Prescott (1978) for the deformations in an elastic lithosphere layer lying over a viscoelastic asthenosphere half-space. A conceptually similar, but mathematically distinct, model was developed by Spence and Turcotte (1979) whose analysis yields similar results. The Savage and Prescott model, which we will discuss in more detail below, serves as the basic viscoelastic half-space asthenosphere model for our comparisons with other models. These early papers pioneered the extention of elastic models of the earthquake cycle to include viscoelastic flow at depth. Since their publication there have been a number of papers in which the vertical and horizontal variation of rheological properties has been more complicated than an elastic layer over viscoelastic half-space. Prominent among these are the thin asthenosphere model of Lehner and Li (1982) and a model with a thin lithosphere near the fault and thicker one further away (Yang and Toksoz, 1980). The latter model is called the varying lithosphere model in this paper. These models, along with some variations, will be the subject of the comparisons discussed here. Other relevant work has focused on viscoelastic inclusions in subduction zones (Wahr and Wyss, 1979), an intracrustal low-viscosity zone (Turcotte, et.al., 1983), viscoelasticity both within the lower lithosphere and asthenosphere (Cohen, 1982), power law flow within the asthenosphere (Melosh and Raefsky, 1983), and sea anchor effects of subducting slabs (Melosh and Fleitout, 1982). All of the

aforementioned models use viscoelasticity as the mechanism for time varying deformation rates. Models involving time varying aseismic slip are also important, particularly in modeling postseismic rebound. There is, however, a so far unresolved ambiguity in distinguishing between elastic slip and viscoelastic flow at depth on the basis of surface geodetic measurements. Finally it may be important in some locales to take into account distributed yielding and the interaction of multiple faults . An analysis similar to ours could be made for dip-slip faults by building on the modeling work of Bischke (1974), Thatcher and Rundle (1979), and Savage (1983).

MODELS AND TECHNIQUES

The comparisons that we will present here are based on the four viscoelastic models and one elastic model shown in Figure 1. In each case there is a vertical strike-slip fault that extends from the surface down to a depth D. The fault penetrates all or part of an elastic layer which we identify with the crust or lithosphere. In the simple elastic half-space model this elastic layer extends to infinite depth. In the viscoelastic half-space model the elastic layer extends from the surface to a depth H ($H \geq D$) where a viscoelastic half-space begins. This low viscosity layer is identified with the asthenosphere or an intracrustal decoupling layer within the lithosphere. Whereas in Figure 1b, the low viscosity layer is a half-space, in Figure 1c it has finite thickness. The new parameter introduced in this thin channel asthenosphere model is the asthenosphere thickness, ΔH. While this model allows for some vertical variation in the viscosity structure, other models have allowed for lateral variations. One such model, the varying lithosphere model, is show in Figure 1d. Here the lithosphere is thinner in the

vicinity of the fault and thickens farther away. The parameters introduced by this model are the lithosphere thickening, ΔL and the half-width of the near-fault, thin lithosphere zone, W. Finally Figure 1e is one example of lateral and vertical confinement of the low viscosity zone. This inclusion model is defined by the half-width parameter, w, and the thickness parameter, ΔH.

The technique we use to compute surface crustal deformations comes from a finite element adaptation of the procedure used by Savage and Prescott (1978) for analyzing the repetitive cycle of earthquakes on strike-slip faults. The displacements attributable to a single episode of strain accumulation and release are decomposed into two contributions. The first contribution is due to block motion of the lithosphere at a constant velocity, v. The second contribution comes from backward fault creep from the surface to depth, D, at velocity, v. The backward creep starts at time zero and continues until the earthquake occurrence (recurrence) time, T. At T an earthquake occurs resulting in a relative displacement across the fault of $\Delta U = 2vT$. Strain accumulated prior to the earthquake is relieved by the coseismic slip. Considering the combined contributions of the two components, the fault is locked at at all times before an earthquake as the two terms cancel. At the time of the earthquake a sudden relative displacement occurs across the fault; subsequently the fault is again locked. A sequence of recurring earthquakes is generated by superposing the time dependent deformations from individual earthquake cycles appropriately shifted in time from one another. The degree to which the nth earthquake cycle in a sequence contributes deformation later in the sequence depends on the ratio between the recurrence time for earthquakes and the relaxation time of the viscoelastic medium. The finite element code that we use in

implementing the models has been discussed in previous papers (e.g. Cohen, 1982). We employ a two dimensional, three degrees of freedom, antiplane strain analysis. The rheological representation used for the viscoelastic elements is a Maxwell fluid in shear and elastic solid in bulk. The Maxwell relaxation time, τ, is defined by $\tau = 2\eta/\mu$ where η is the viscosity and μ the rigidity of the viscoelastic material. To facilitate comparisons with earlier work, the depth of the coseismic slip plane D will be taken to be the bottom of the elastic layer, H (D = H in Figures 1b to 1e). Except in the special cases discussed later, the dimensions of the finite element grid are chosen to be large compared to all other dimensions discussed in this paper. This assures that the boundary conditions at the sides and the bottom of the grid do not effect the results. Explicit integration of the constitutive equations is employed with the integration step size chosen to be small compared to the Maxwell time of the viscoelastic material.

It follows from the preceeding discussion that the displacement, u(t), at time t can be written:

$$u(t) = vT + u_2(t) + \sum_{m=1}^{\infty} [u_2(t+mT) - u_2(mT)]. \qquad (1)$$

In this equation the first term is the displacement due to the block motion and does not contribute to the stress or strain field. The second term is the contribution to the crustal deformation from the coseismic slip and the aseismic backward creep during the current earthquake cycle. The terms under the summation sign arise from the viscoelastic response to slip and backward creep during earlier cycles. For an elastic earth each of the difference terms (for a given m) would be exactly zero. In addition for an elastic earth $u_2(T) = 0$. Figure 2 shows how the viscoelastic flow in the asthenosphere alters this behavior.

Results are shown for both half-space and thin channel asthenospheres. Here the individual difference terms are no longer zero. The higher order terms in the viscoelastic response become of greater relative importance as distance from the fault increases. Also the higher order terms have a somewhat greater significance at most locations in the thin asthenosphere model than in the half-space case. That the overall amplitude of the viscoelastic effect in the thin channel model is less than in the half-space model is also apparent. Summing together all the contributions to the displacements we generate a set of curves for the displacements as a function of distance from the fault and time between earthquakes as shown in Figure 3. For the viscoelastic models, postseismic displacements (e.g. $t/T = 0.2$) at intermediate distances from the fault not only exceed those in the near and far fields but also change with a velocity greater than the uniform translation rate of the loading blocks. This accelerated motion is a common characteristic of the postseismic rebound. To make this point more explicit we show in Figure 4 a sample plot of velocity, u, versus distance at various times. Notice that at $t/T = 0.1$ the velocity at $X/D = 2$ exceeds that at great distances from the fault by over 50 percent. At some later times in the earthquake cycle, however, the velocity is considerably slower than that for an elastic earth.

Let us now turn to a more detailed comparison of the thin channel and half-space asthenosphere results. Examples of the displacement patterns are compared in Figures 3c and 3d. Compared to the half-space asthenosphere model, the displacements in the thin channel model are reduced in amplitude for all times $t < 1$. The differences between the two models are greatest early in the cycle, when viscoelastic effects are most pronounced, and progress toward zero as the recurrence time is approached. The location of the peak in the displacement pattern marks the

boundary between a zone of positive shear strain near the fault and negative shear strain farther away. The width of the zone of positive strain increases with time and eventually encompasses the entire region shown in the figure. For the thin channel model the location of the point of greatest displacement is displaced faultward. This reflects the general confinement of the zone of significant deformation (high strain) closer to the fault. Toward the end of the cycle, however, the deformation field approaches that for a half-space asthenosphere. Figure 5 shows an example of the variation in displacement at X = D as ΔH increases. For example with $t/T = 0.2$, $u/\Delta U = 0.05$, 0.10, and 0.12 for $\Delta H/D = 0$, 1, and 4 and respectively. The latter value is close to the half-space asthenosphere value.

Since strain rates rather than displacements are the quantities most readily deduced from most multilateration measurements we will, henceforth, focus most of our attention on a comparison of computed strain rates. Examples of representative engineering shear strain rates, $\dot{\epsilon}$, are shown as a function of distance from the fault, X, and at two times in Figure 6. The primary observation that can be made about the strain rates in the two models is that they are in fairly good agreement. This is true despite the fact that the thickness of the low viscosity layer in the thin asthenosphere model is fairly small, i.e., $\Delta H = H$. On a closer examination, however, we find that there are some important second order differences between the models. In the near-field, the strain rates after the earthquake are somewhat reduced when the asthenosphere thickness is decreased. The situation is reversed toward the end of the earthquake cycle. Thus the near-field strain rates go through a greater range of values as the asthenosphere thickness increases. Furthermore the minima in the postseismic strain rate patterns vary in both magnitude and location with the asthenosphere

thickness. We focus on these differences in the next two figures and discuss those circumstances for which the thickness of the low viscosity zone might be estimated from comparisons of calculations and observations. Figure 7 shows the dependence of the near-field (X/D=0.025) postseismic strain rates on the asthenosphere thickness $\Delta H/D$. The normalized strain rate, $\dot{\epsilon}/(\Delta U/DT)$, rises rapidly from its elastic value (when $\Delta H = 0$) of 0.3 to near the half-space asthenosphere value of just over 1 as ΔH increases. Even for the very modest value of asthenosphere thickness for which $\Delta H = D$, $\dot{\epsilon}/(\Delta U/DT) = 0.9$ and for $\Delta H/D > 1$ the strain rate is nearly the half-space value. Thus measurements made in the near-field are sensitive to the asthenosphere thickness only over a narrow range of values. If the thickness is more than about one fault depth, the shear strain is close to that obtained with a half-space. Measurements made farther away from the fault have a somewhat greater relative sensitive to the asthenosphere thickness. Figure 8 shows how the magnitude, $\dot{\epsilon}_m$, and location, X_m, of the minimum in the postseismic strain rate pattern (at a fixed time) vary as a function of asthenosphere thickness. The magnitude increases (in an absolute value sense) as asthenosphere thickness increases until $\Delta H/D > 1$ then slowly decreases toward the half-space value of approximately -0.7. Thus for most values of asthenosphere thickness the minimum is deeper than that predicted for the half-space. The position of the minimum differs markedly from that for a half-space when the asthenosphere thickness is less than about 3D. For example with D =20 km., X_m = 50 km., 65 km., and 72 km. for ΔH = 20 km., 40 km., and infinity respectively. The position of the minimum for the half-space model is almost 50 percent further from the fault than it is for $\Delta H/D = 1$. Note also that the position of the minimum moves away from the fault rapidly for $\Delta H/D < 1$ as elastic behavior is approached and the extremum disappears.

The results presented above were obtained with the ratio of the earthquake recurrence time to Maxwell relaxation time equal to five, i.e., $T/\tau = 5$. We have rerun a few of our calculations with $T/\tau = 20$ to see how decreasing the asthenosphere viscosity effects these results. As was expected the postseismic displacements are greater when the viscoelastic relaxation is more rapid. Therefore the development of the peak in the postseismic displacement pattern at intermediate distances from the fault is more pronounced. The postseismic strain rates increase roughly linearly with T/τ. Associated with the increase in the postseismic strain rates near the fault is a decrease in the rates later on; thus the greatest fraction of the straining before an event in an earthquake sequence occurs shortly after the preceeding event in the sequence. The strain rate in the near-field undergoes an increasing time variation when the viscosity of the asthenosphere decreases. Even though the postseismic strain rates are increased with the more rapid viscoelastic response, we still find that the near-field strain rate becomes 90% of the half-space asthenosphere result when $\Delta H/D > 1.75$. This is because the postseismic strain rates increase with a reduction in viscosity for both the thin channel and half-space asthenosphere models.

One of the most important findings of this study is that the effect of having a finite width asthenosphere is much different from that predicted by the recent analytic approximations of Lehner and Li (1982). Their model predicts displacements which are generally much greater than that for a half-space asthenosphere (when $X/D < 7$), whereas we have found smaller displacements when the asthenosphere has a finite width. In addition Lehner and Li find that deviations from half-space asthenosphere behavior occur over a much larger range of asthenosphere thickness than are indicated by the finite element

calculations. For example, with $\Delta H/D = 5$, they find that the displacements at $t/\tau=0.2$ are as much as 40% bigger than that predicted by the half-space asthenospere model. On the other hand, we find the displacements are close to that predicted by the half-space asthenosphere model and slighly smaller. After performing a number of numerical experiments we now believe that we understand at least some of the difficulties with the Lehner and Li model. Their model is a two-layer approximation with the material below the asthenosphere ignored. The mathematical development of the model utilizes thickness averaged deformation and stress variables and ignores some of the shear stresses within the asthenosphere. As the authors point out, the model is most suspect near the fault, the region where the greatest crustal deformation occurs. The authors also indicate that the model may be inaccurate at large distances from the fault. We have attempted to mimic the calculations of Lehner and Li by using their choice of viscosity, rigidity, earthquake recurrence time, layer thickness, etc. in a number of calculations. One of these calculations is a a two-layer calculation using finite elements with the bottom boundary of the finite element grid held fixed for the calculation of u_2. In a second case, the same calculation is performed with the bottom boundary made free. In a third calculation we use our three layer model with elastic material extending from the bottom of the asthenosphere to a great depth (the choice of the boundary condition at the bottom of this grid is immaterial). We have also reproduced the analytic calculations and performed calculations using a half-space asthenosphere model. (In the latter case several different techniques yield substantially the same result. In redoing the analytical calculation a sign error was corrected in the published equations, but this error has not affected the figures.) A comparison of these five calculations is shown in Figure 10. We see that the analytical model predicts the

greatest displacements. The smallest displacements are predicted by the three layer model and the two layer model with the bottom boundary held fixed (these two calculations are in very close agreement). In addition the three layer results are fairly close to and a little smaller than the half-space asthenosphere results as expected from our earlier analysis. Interestingly the free boundary, two-layer model yields displacements which are somewhat greater than the half-space asthenosphere displacements. The free boundary condition results are the closest results we have obtained to the analytical model, but the agreement between the two is still not satisfactory. The results obtained with a free (fixed) boundary can also be obtained using a three layer model with a low (high) rigidity elastic layer below the asthenosphere. The validity of the finite element calculations is confirmed not only by checking with independent calculations in the half-space asthenosphere limit, $\Delta H = \infty$, but also by verifying the smooth transition to elastic behavior as ΔH approaches zero. On the basis of these calculations we conclude that the enhanced displacements predicted by the analytical model result from model simplifications that are unlikely to occur in nature, such as ignoring the presence of material below the asthenosphere and averaging variables over the fault depth. Despite the fact that the displacements are smaller in the thin channel model than in the half-space asthenosphere model, we find that the minima in the postseismic strain rate pattern are deeper as indicated earlier in Figure 8.

Before leaving consideration of the finite width asthenosphere model we examine how the half-width of the strain rate field varies with time. We define the half-width, $X_{1/2}$, as the distance from the fault at which the strain rate is one-half its maximum, near-fault value. The width increases with time, an example being shown in Figure 11. In general the growth in the width of

the strain field accelerates with time following an earthquake as the near-field strain rates decrease and the far-field values increase. The details of the growth depend on the thickness of the asthenosphere. Just after an earthquake the width of the strain rate field and its time rate of change are comparable for the half-space asthenosphere and the thin layer asthenosphere models. As time passes, however, the growth rate for the half-space asthenosphere model increases more rapidly.

The next model we consider, the varying lithosphere model, is shown in Figure 1d. For distances from the fault $X > W$ the lithosphere thickness is H. At greater distances from the fault the thickness is $H + \Delta L$. As an illustrative case we take $W = D$ and $\Delta L/D = 1.5$ (with $H/D = 1$ and $T/\tau = 5$). In Figure 12 we once again see that the strain rate curves for this model and the half-space asthenosphere model are quite similar but there are some important differences. The postseismic near-field strain rates are less in the varying lithosphere model. Toward the end of the earthquake cycle these strain rates are greater. As for the spatial pattern, the strain rates at intermediate and far-field distances show less variation with distance from the fault than do the corresponding strain rates for the half-space model. This is because the lithosphere is thicker at these greater distances and the deformation pattern takes on some of the aspects of an elastic field. As in the previous case it is informative to examine how the magnitude of the near- and intermediate-field postseismic strain rates vary with the model parameters. Figure 13 shows the variation in the near-field rate with width and thickening. Strain rates within 90% of the half-space asthenosphere value are achieved whenever the width of the thin lithosphere zone exceeds one-and-a-half times the fault depth, D. Similarly whenever the distant thickening of the lithosphere is less than 50%, the strain rates are 90% or greater

of the half-space asthenosphere value. As to the location and magnitude of the postseismic strain rate minima, the results are shown in Figure 14. Four points should be noted. First when the width, W/D, is small the magnitude and position of $\dot{\epsilon}_m$ depend strongly on thickening, $\Delta L/D$. Second when the width is greater than about 3D nearly half-space asthenosphere behavior is achieved independent of the value of ΔL. Third, when the thickening of the lithosphere away from the fault zone exceeds three times the fault depth, then ϵ_m and X_m depend strongly on W (for $W/D < 3$). Fourth, at the small lithosphere thickening value of $\Delta L = 0.5D$, $\dot{\epsilon}_m/(\Delta U/DT)$ increases from -.05 to -.71. as W/D increases from two to infinity. The location of the minimum, X_m/D, decreases from 4.9 at $W/D = 0.5$ to about 3.5 for W/D equal to 2.0 and 3.75 and varies only slightly thereafter.

The final model we investigate is somewhat of a hybrid of the preceeding two models. Here viscoelastic flow is confined to a rectangular inclusion located symmetrically about the bottom of the rupture tip. The inclusion width, ΔH, is analogous to the layer thickness for the thin layer asthenosphere model; the inclusion half-width is w. Figure 15 shows representative calculations of the strain rate for this model with $\Delta H/D = 1.5$ and $w/D = 1$. The viscoelastic features are still present but somewhat muted compared to the half-space asthenosphere result. Particularly noticeable are the decrease in the postseismic near-field strain rates, the poorer development of the postseismic intermediate and far-field negative strain rate pattern, and the higher strain rates in the near field toward the end of the earthquake cycle. These are all effects we have seen in other models with finite dimensions for the asthenosphere. Figure 16 provides information on how the near-field strain rate approaches the half-space asthenosphere result as ΔH and w increase. Basically we find that when the thickness and the half-width are

greater than about one or two times the fault depth, then the near-field strain rates are close to the half-space results. On close inspection of the results, such as those presented in Figure 15, we are again led to the conclusion that the best hope for determining the asthenosphere structure comes from making very accurate measures at distances up to several times the fault depth away from the fault.

SUMMARY

We have examined the strain rates and, to a lesser extent, the displacment patterns associated with several different linear viscoelastic models of the earthquake cycle. These models differ in the geometric structure assumed for the subsurface viscoelastic material. Generally we find that when the viscoelastic material has an extent greater than a few times the fault depth, then the crustal deformation pattern looks very much like that obtained when the viscoelastic region is a half-space. In this case it is difficult to determine information about the vertical or lateral structure of the low viscosity zone. On the other hand, when the low viscosity zone extends over a smaller domain in either a vertical or lateral direction then geodetic measurements might be used to distinguish among models and determine the geometric structure of the asthenosphere. Although such a determination will not be unique, the greatest amount of information will come from geodetic surveys made shortly after an earthquake (when the viscoelastic effects are greatest) and at distances away from the fault up to several times the fault depth (where model differences are most important). Among the features predicted by the finite element viscoelastic calculations is that the confinement of viscoelastic flow to a finite thickness channel reduces the displacements over that expected for a

viscoelastic half-space. Indications to the contrary based on analytic work are the result of ignoring the presence of high viscosity material below the viscoelastic channel and using thickness averaged variables which are inapplicable near the fault.

REFERENCES

Bischke, R.H., 'A model of convergent plate margins based on the recent tectonics of Shikoku, Japan,' J. geophys. Res., 79, 4845-4857, 1974.

Cohen, S.C., 'A multilayer model of time dependent deformation following an earthquake on a strike slip fault,' J. geophys. Res., 87, 5409-5421, 1982.

Hadley, D. and Kanamori, H., 'Seismic structure of the Transverse Ranges, California,' Bull. Seismol. Soc. Am., 88, 1769-1771 1979.

Lehner, F.K. and Li, V.C., 'Large scale characteristics of plate boundary deformation related to the postseismic readjustment of a thin asthenosphere,' Geophys. J. R. astr. Soc., 71, 775-792, 1982.

Melosh, H.J. and Fleitout, L., 'The earthquake cycle of subduction zones,' Geophys. Res. Lett., 9, 21-29, 1982.

Melosh, H.J., and Raefsky, A., 'Anelastic response of the earth to dip-slip earthquakes,' J. geophys. Res., 88, 515-526, 1983.

Savage, J.C. and Prescott, W.H., 'Asthenosphere readjustment and the earthquake cycle,' J. geophys. Res., 83, 3369-3376, 1978.

Savage, J.C., 'A dislocation model of strain accumulation and release at a subduction zone,' J. geophys. Res., 88, 4984-4996.

Spence, D.A. and Turcotte, D.L., 'Viscoelastic relaxation of cycle displacements on the San Andreas Fault,' Proc. Roy. Soc. A., 365, 121-149, 1979.

Thatcher, W. and Ruudle, J.B., 'A model for the earthquake cycle in underthrust zones,' J. geophys. Res., 84, 5540-5550, 1979.

Turcotte, D.L., Liu, J.Y., and Kulhawy, F.H., 'The role of an intracrustal asthenosphere on the behavior of major strike slip faults,' submitted for publication, 1983.

Wahr, J. and Wyss, M., 'Interpretation of postseismic deformation with a viscoelastic relaxation model,' J. geophys. Res., 85, 6471-6477, 1980

Yang, M. and Toksoz, M.N., 'Time dependent deformation and stress relaxation after strike slip earthquakes,' J. geophys. Res., 86, 2889-2901, 1981.

FIGURE CAPTIONS

Figure 1: Models used in earthquake cycle simulations:
a. Elastic half-space model
b. Viscoelastic half-space asthenosphere model
c. Viscoelastic thin-channel asthenosphere model
d. Viscoelastic varying lithosphere model
e. Viscoelastic inclusion model.

Figure 2: Superposition of multicycle displacement fields for thin channel and half space asthenosphere models.

Figure 3: Displacements versus distance from the fault at various times for several different models:
a. Elastic model
b. Viscoelastic half-space asthenosphere model
c. Viscoelastic thin channel asthenosphere model.

Figure 4: Velocity versus distance from the fault at various times for half-space asthenosphere model.

Figure 5: Displacement at X/D = 1 and at various times versus thickness of asthenosphere channel.

Figure 6: Strain rate versus distance from the fault at various times for half-space and thin channel asthenosphere models.

Figure 7: Near-field, postseismic strain rate versus asthenosphere thickness for thin channel asthenosphere model.

Figure 8: Magnitude and location of postseismic strain rate minimum for thin channel asthenosphere model.

Figure 9: Comparison of displacements and strain rates for viscelastic models with different relaxation times.

Figure 10: Half-width of strain rate field versus time for half-space and thin channel asthenosphere models.

Figure 11: Comparison of patterns of displacement versus distance from the fault for thin channel analytic model and finite element models employing various boundary conditions (b.c.) for the calculation of u_2.

Figure 12: Strain rate versus distance from the fault at various times for half-space asthenosphere and varying lithosphere models.

Figure 13: Near-field postseismic strain rate dependence on the width of the thin lithosphere zone and magnitude of the lithosphere thickening.

Figure 14: Magnitude and position of postseismic strain rate minimum for varying lithosphere model.

Figure 15: Strain rate versus distance from the fault at various times for the half-space asthenosphere and inclusion models.

Figure 16: Near-field postseismic strain rate dependence on inclusion width and thickness.

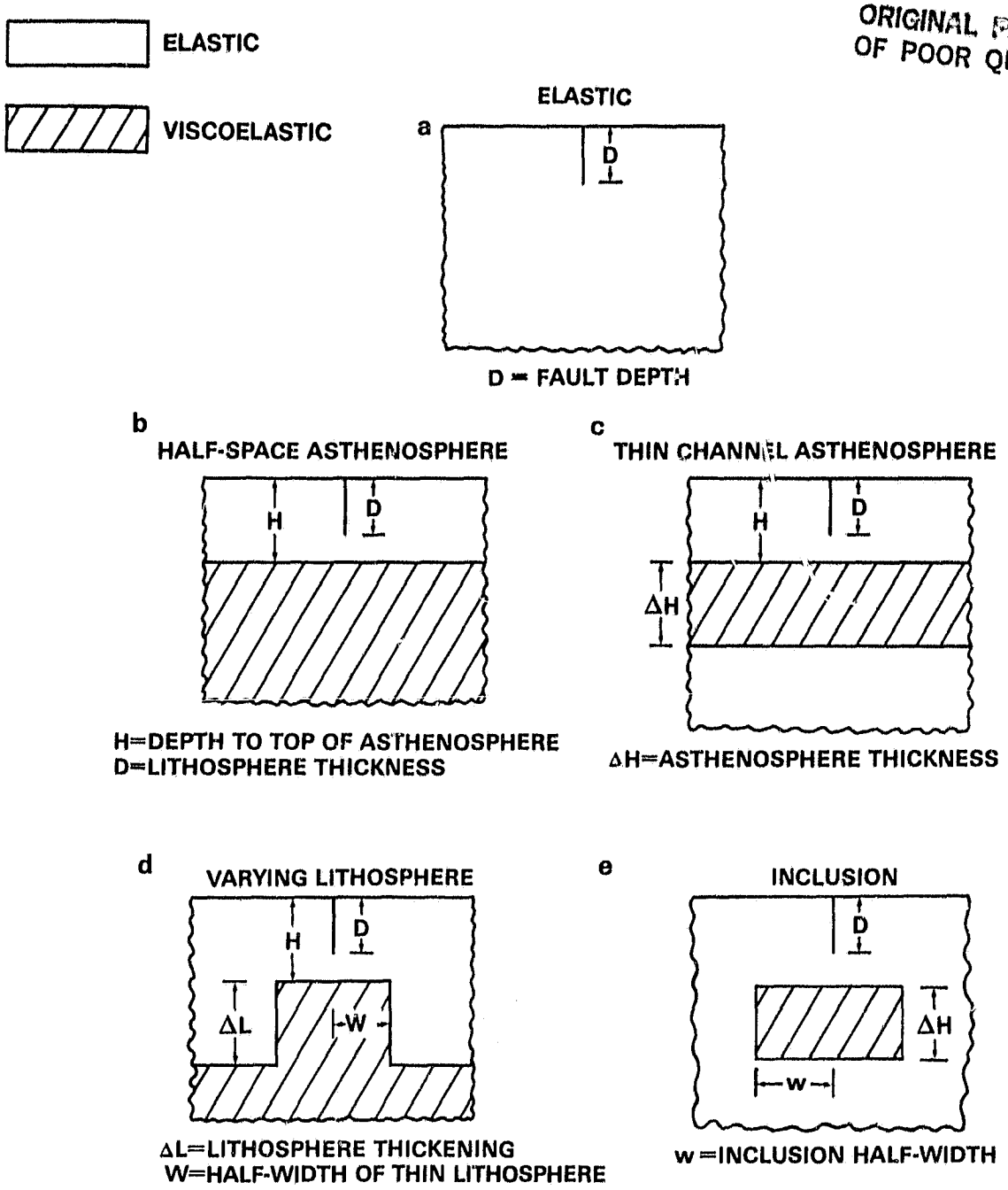

Figure 1: Models used in earthquake cycle simulations:

a. Elastic half-space model
b. Viscoelastic half-space asthenosphere model
c. Viscoelastic thin-channel asthenosphere model
d. Viscoelastic varying lithosphere model
e. Viscoelastic inclusion model.

$$U = vt + U_2(t) + \sum_{m=1}^{\infty} [U_2(t + mT) - U_2(mT)]$$

$H/D = 1 \quad T/T = 5$

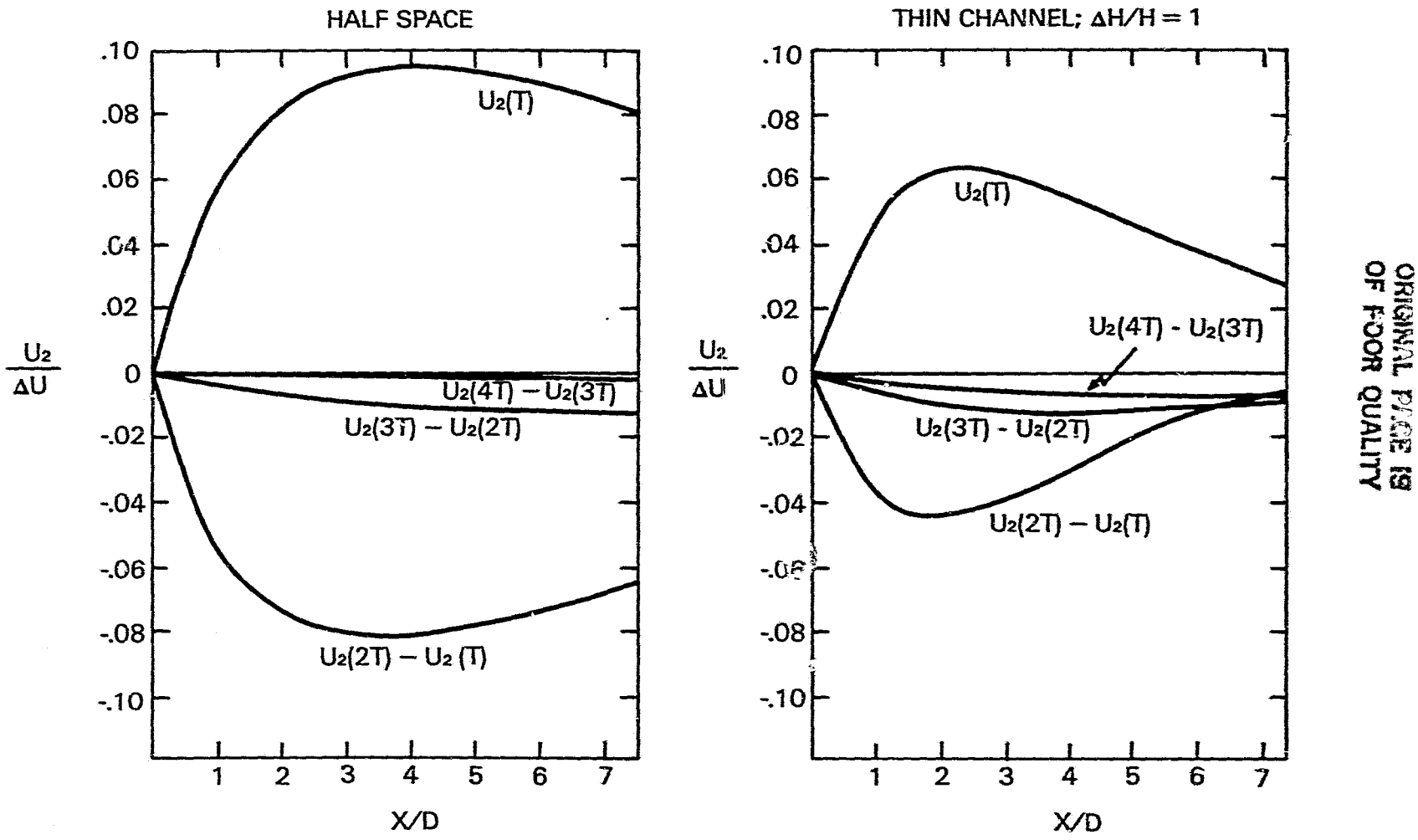

Figure 2: Superposition of multicycle displacement fields for thin channel and half space asthenosphere models.

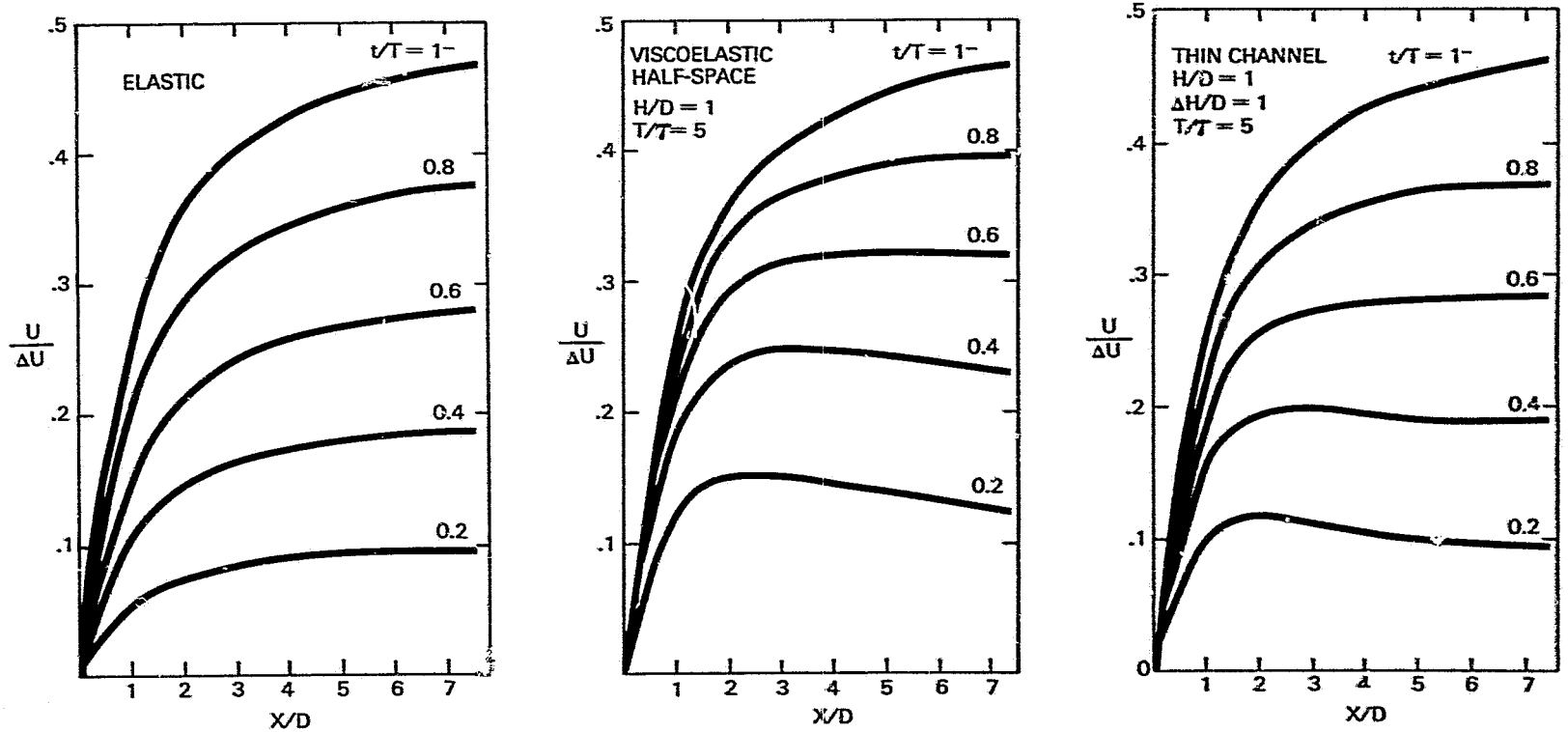

Figure 3: Displacements versus distance from the fault at various times for several different models:

a. Elastic model

b. Viscoelastic half-space asthenosphere model

c. Viscoelastic thin channel asthenosphere model.

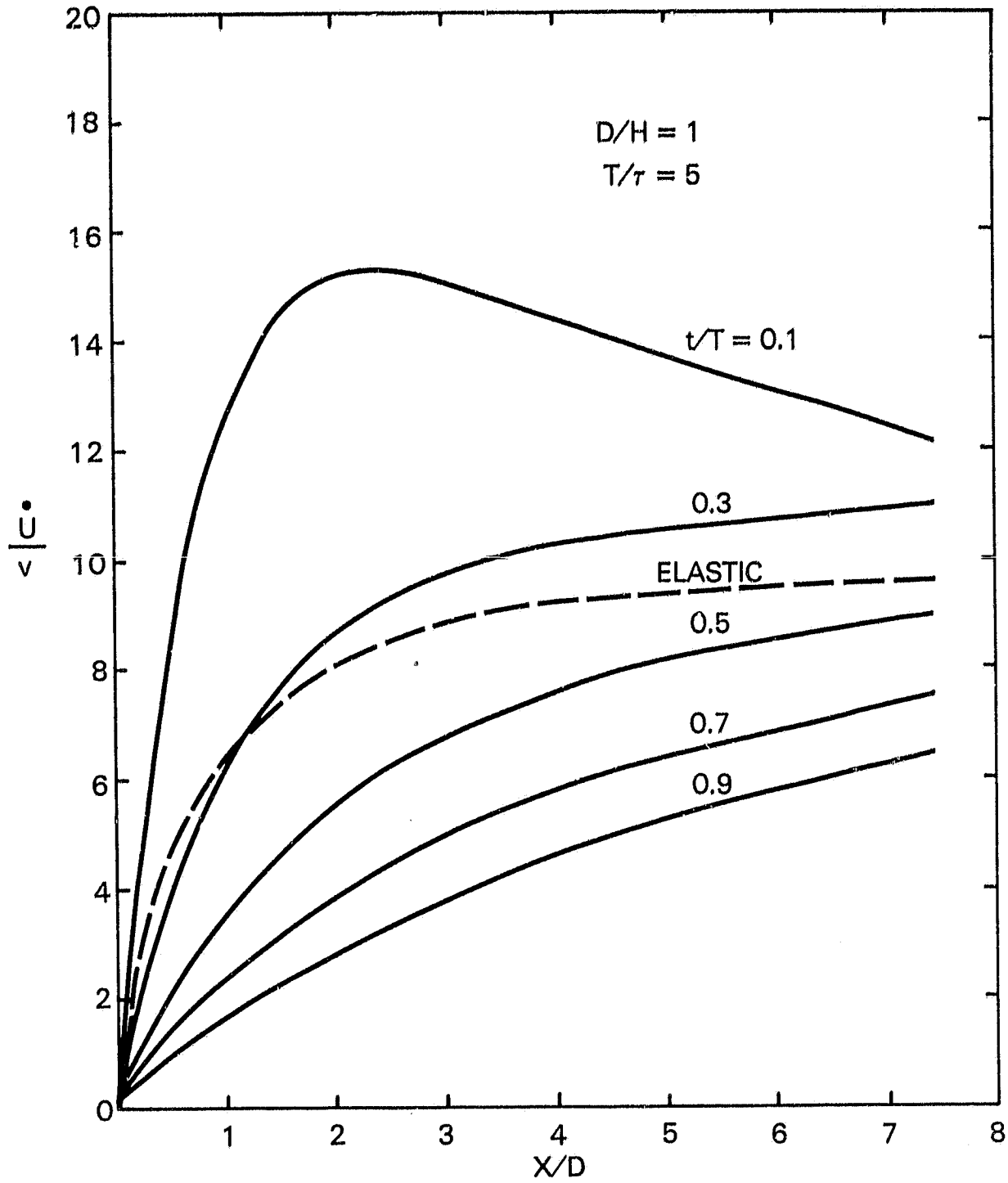

Figure 4: Velocity versus distance from the fault at various times for half-space asthenosphere model.

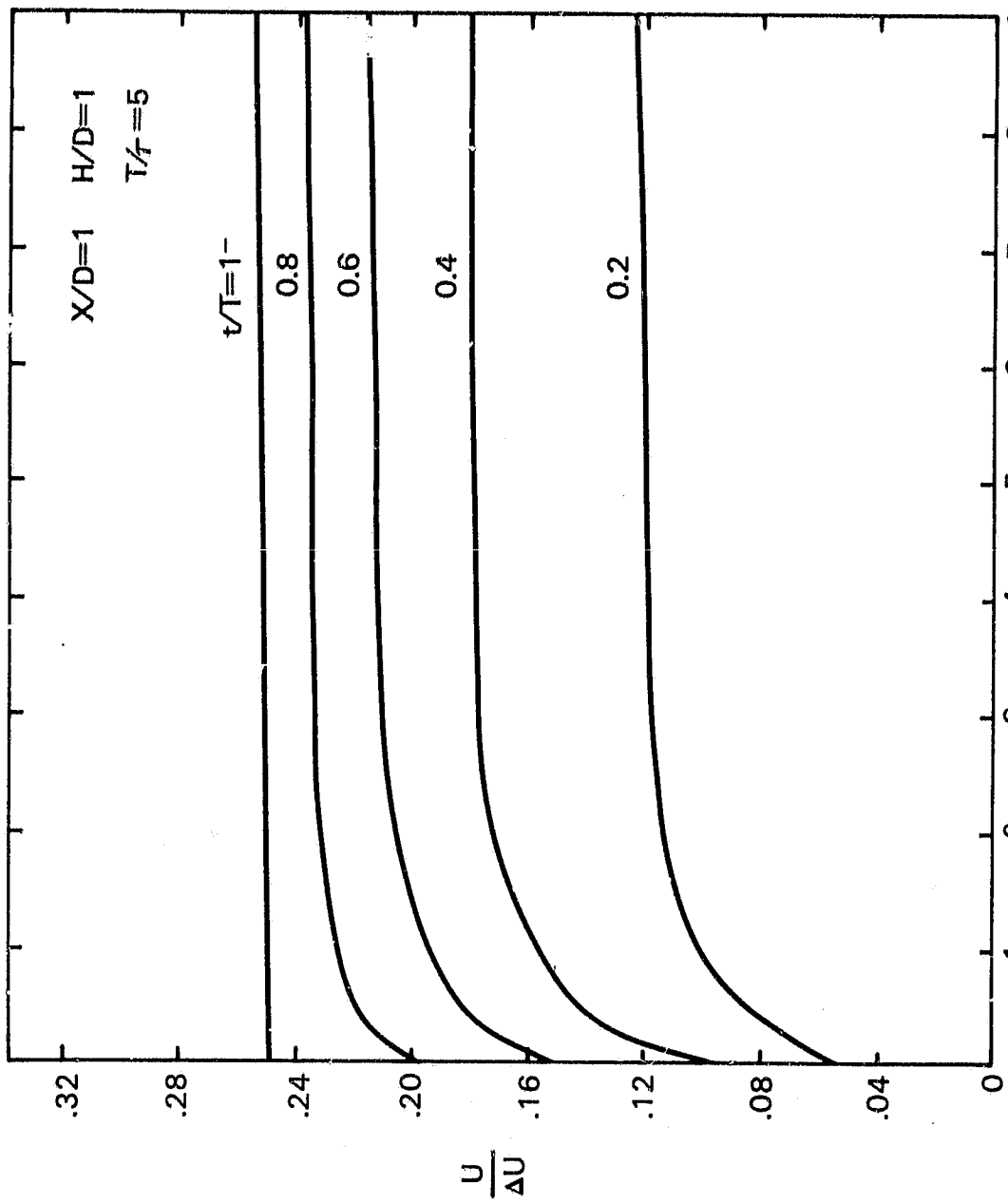

Figure 5: Displacement at X/D = 1 and at various times versus thickness of asthenosphere channel.

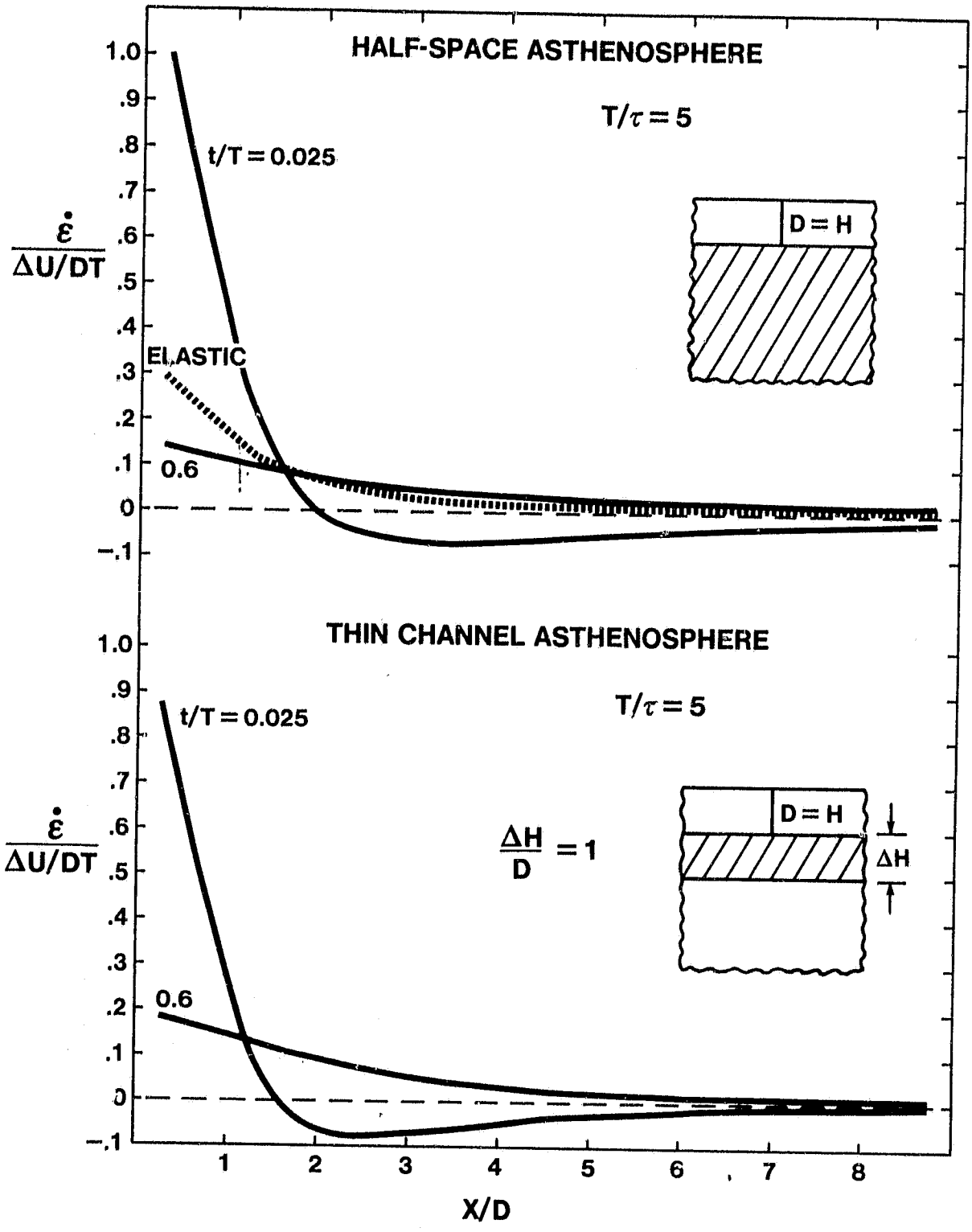

Figure 6: Strain rate versus distance from the fault at various times for half-space and thin channel asthenosphere models.

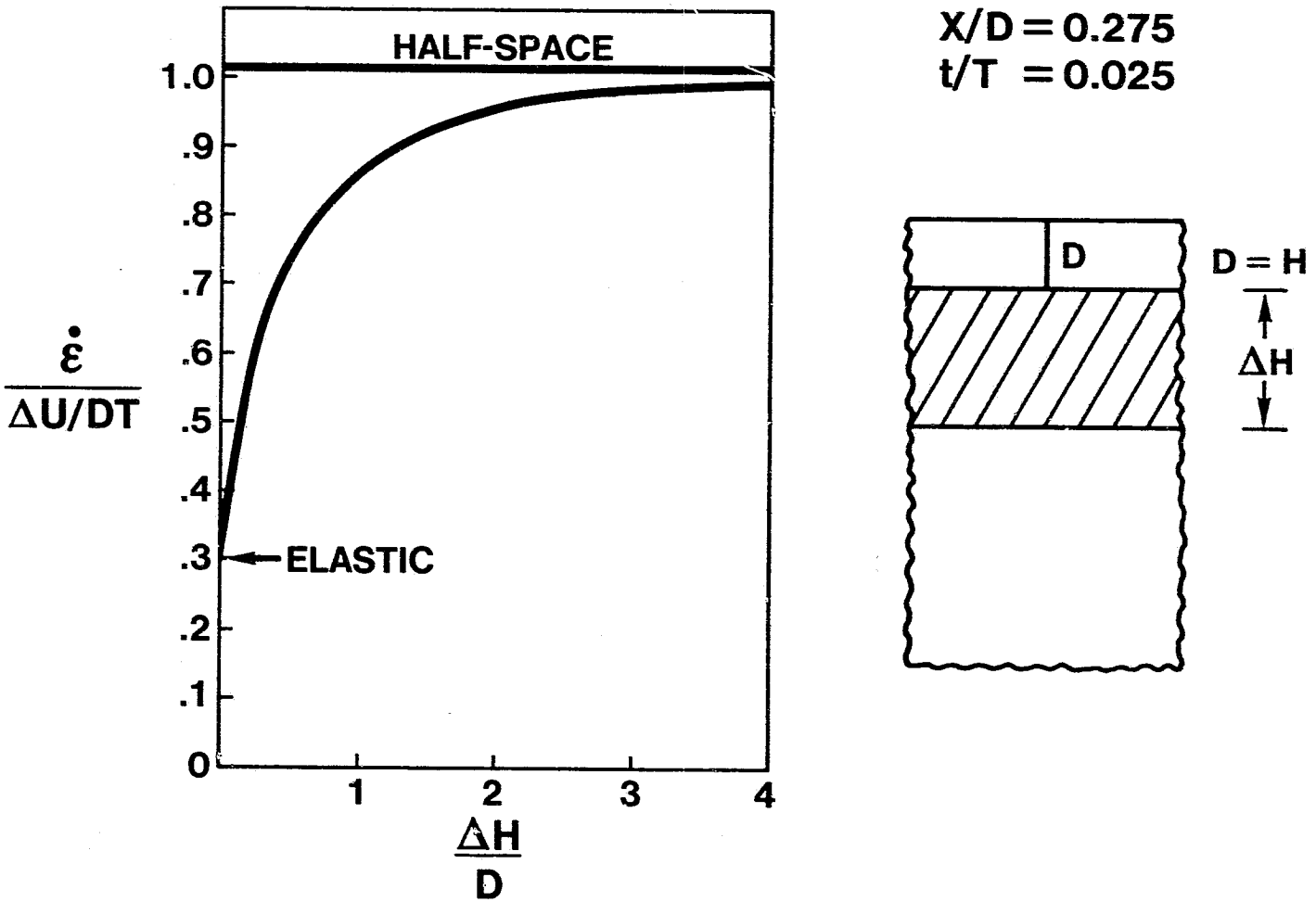

Figure 7: Near-field, postseismic strain rate versus asthenosphere thickness for thin channel asthenosphere model.

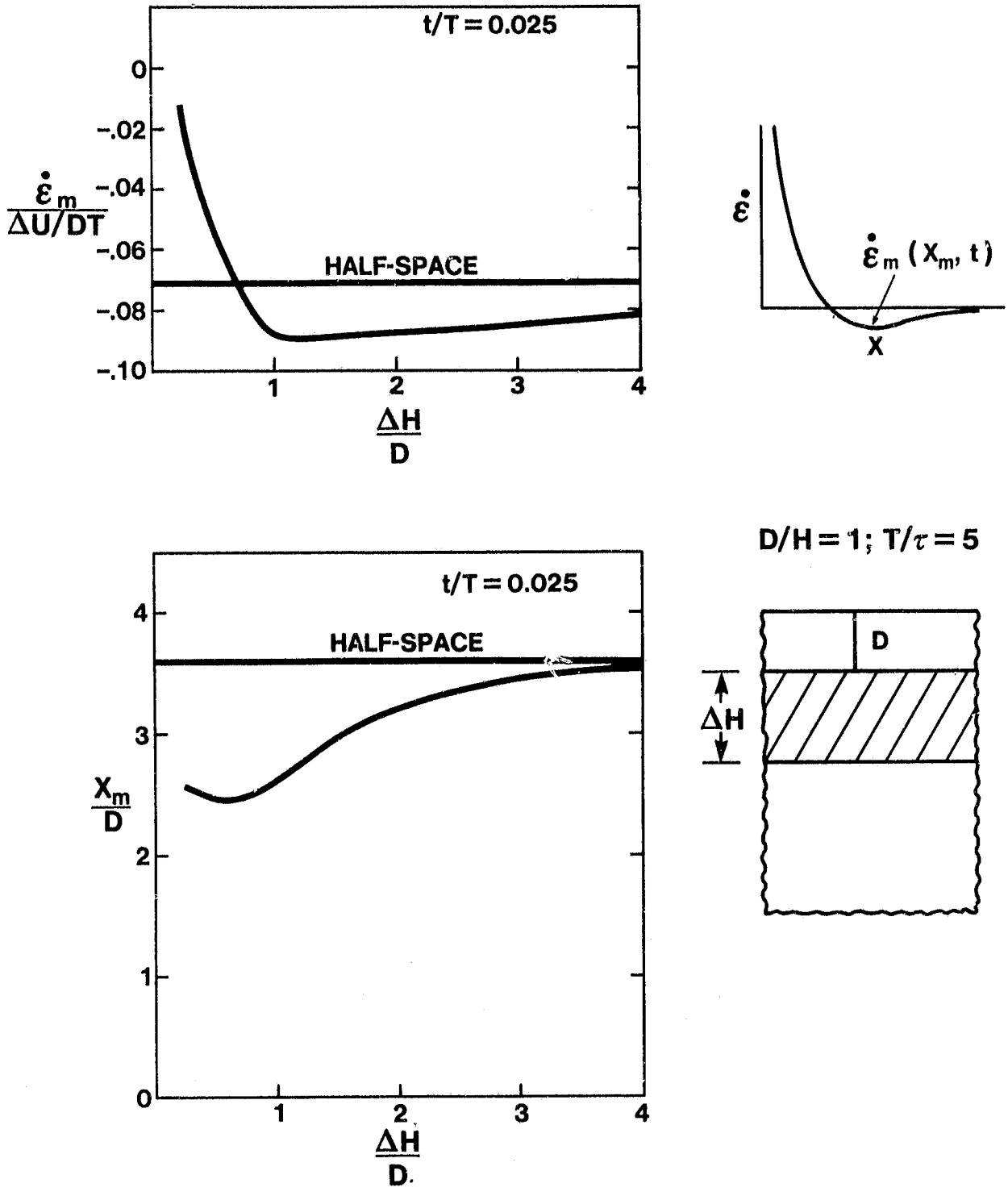

Figure 8: Magnitude and location of postseismic strain rate minimum for thin channel asthenosphere model.

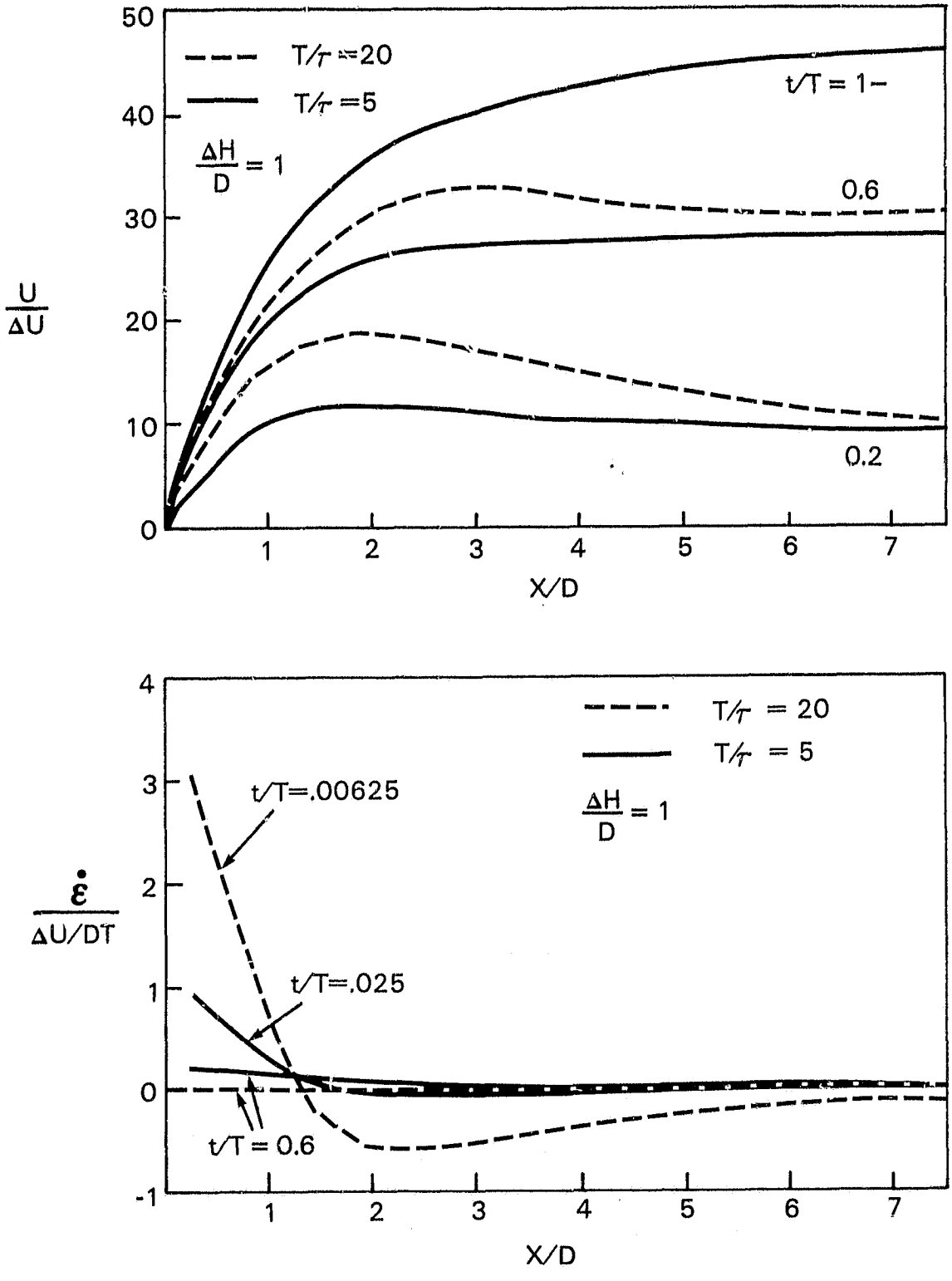

Figure 9: Comparison of displacements and strain rates for viscoelastic models with different relaxation times.

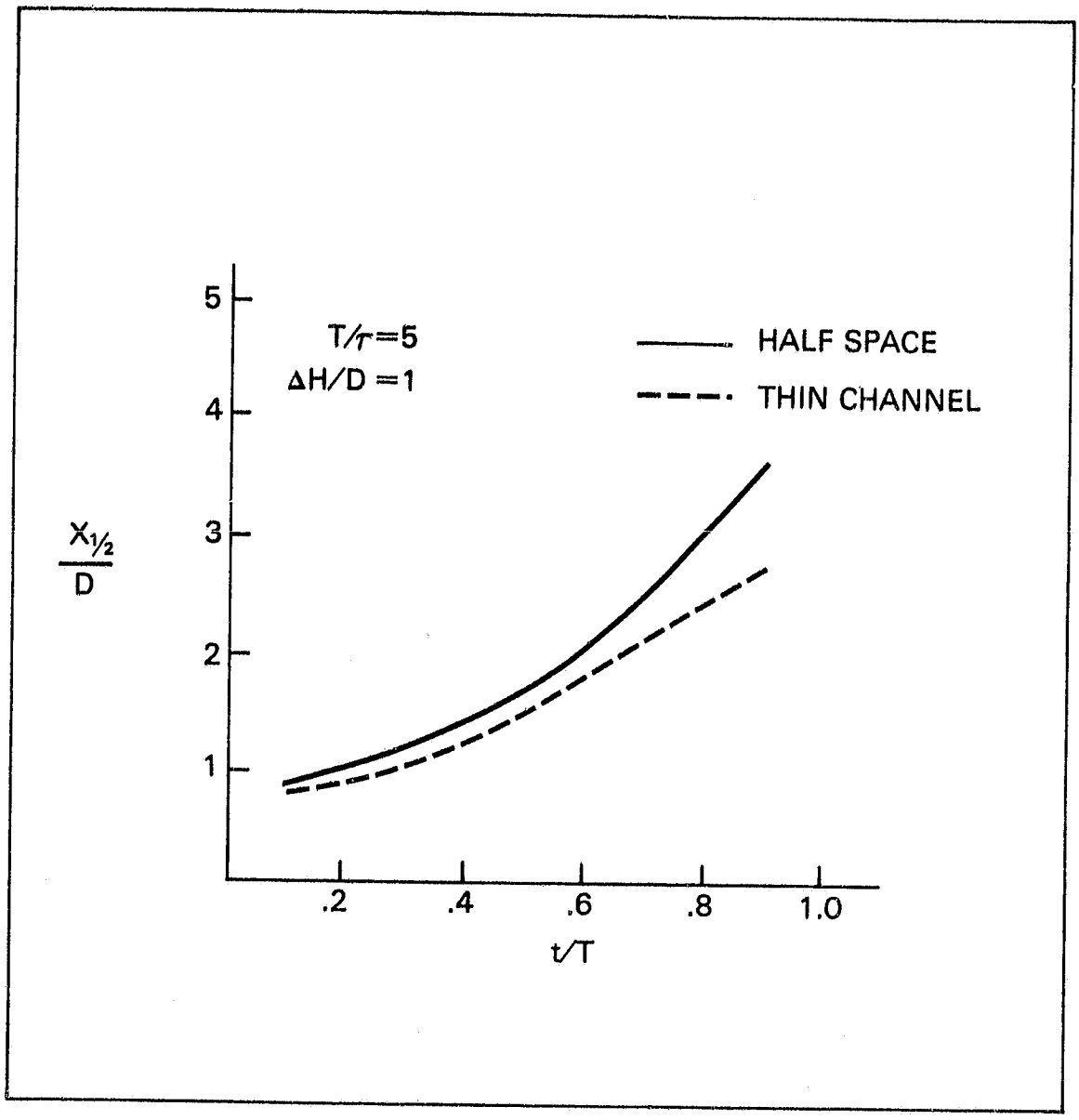

Figure 10: Half-width of strain rate field versus time for half-space and thin channel asthenosphere models.

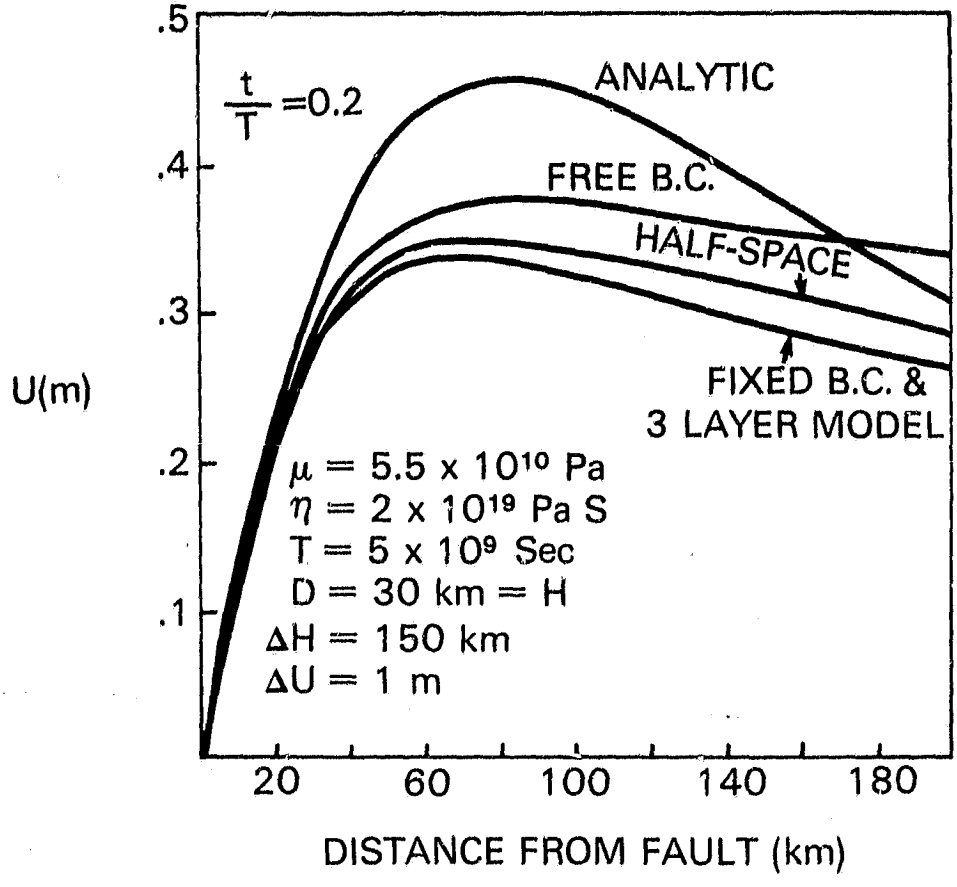

Figure 11: Comparison of patterns of displacement versus distance from the fault for thin channel analytic model and finite element models employing various boundary conditions (b.c.) for the calculation of u_2.

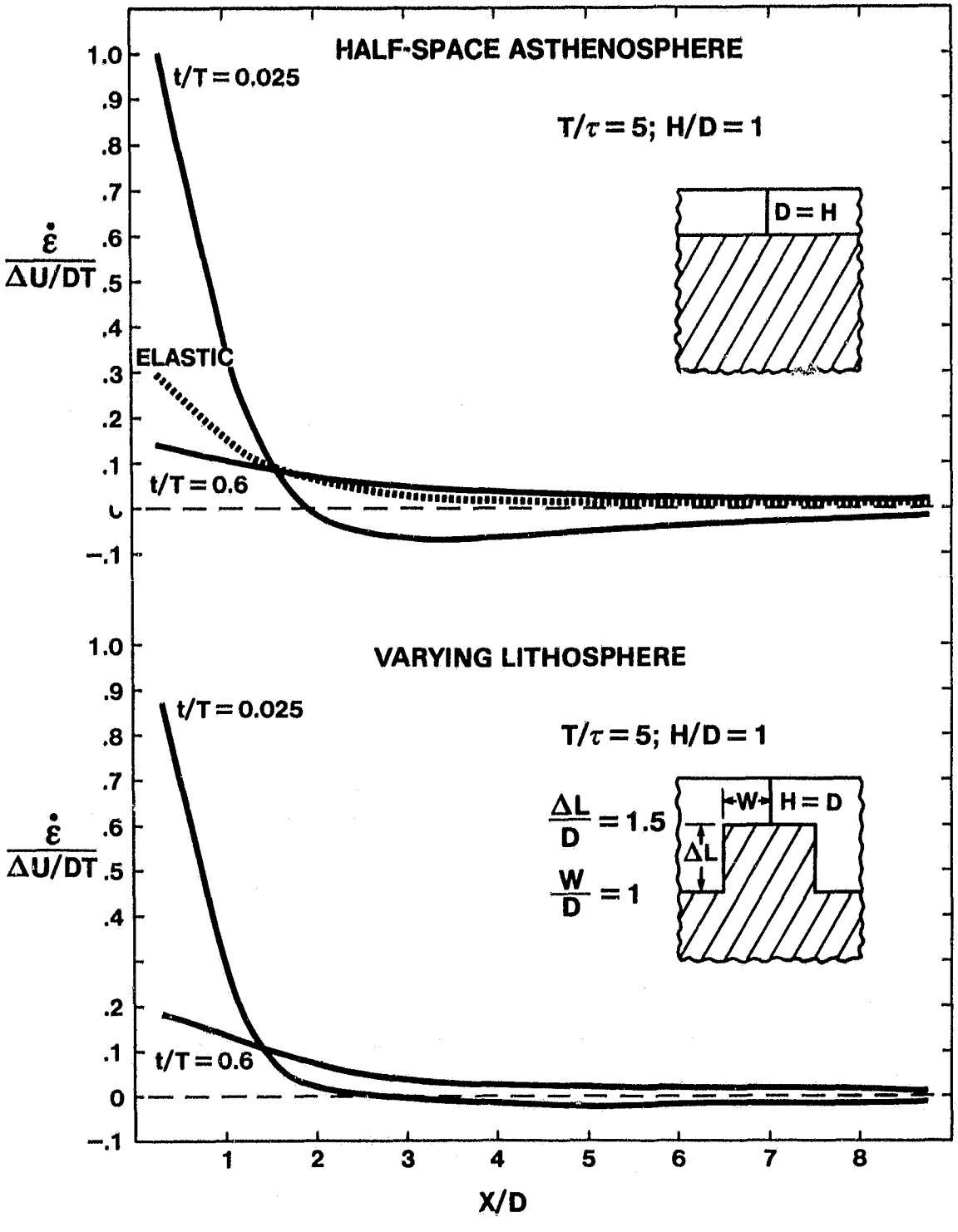

Figure 12: Strain rate versus distance from the fault at various times for half-space asthenosphere and varying lithosphere models.

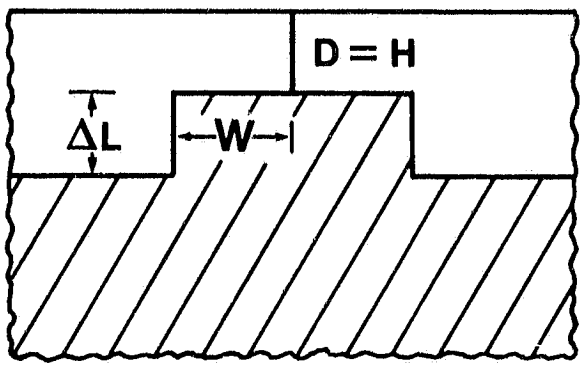

$H/D = 1;\ T/\tau = 5$

$$\frac{\dot{\varepsilon}}{\Delta U/DT}$$

$X/D = 0.275;\ t/T = 0.025$

$\frac{\Delta L}{D}$	$\frac{W}{D}$ = 0.5	1.0	1.5	2.0	3.75	∞
0	1.01	1.01	1.01	1.01	1.01	1.01
.5	.86	.94	.98	1.00	1.01	1.01
1.0	.78	.90	.96	.98	1.00	1.01
1.5	.74	.87	.94	.97	1.00	1.01
2.75	.71	.85	.92	.96	1.00	1.01
4.0	.70	.84	.92	.96	1.00	1.01
∞	.69	.84	.91	.96	1.00	1.01

Figure 13: Near-field postseismic strain rate dependence on the width of the thin lithosphere zone and magnitude of the lithosphere thickening.

$t/T = 0.025$

$\dot{\varepsilon}_m / (\Delta U/DT)$

$\frac{\Delta L}{D}$ \ $\frac{W}{D}$	0.5	1.0	1.5	2.0	3.75	∞
0.5	−.044	−.044	−.044	−.050	−.063	−.071
1.0	−.024	−.028	−.031	−.043	−.064	−.071
1.5	−.018	−.020	−.025	−.059	−.065	−.071
2.75	−.009	−.012	−.043	−.066	−.068	−.071
4.0	−.005	−.018	−.049	−.071	−.070	−.071
∞	−.013	−.029	−.058	−.077	−.070	−.071

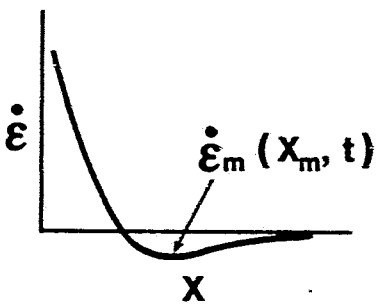

X_m/D

$\frac{\Delta L}{D}$ \ $\frac{W}{D}$	0.5	1.0	1.5	2.0	3.75	∞
0.5	4.9	4.7	4.3	3.5	3.5	3.6
1.0	6.4	5.4	4.7	2.7	3.4	3.6
1.5	7.4	6.7	2.9	2.7	3.4	3.6
2.75	10.5	3.4	2.6	2.5	3.3	3.6
4.0	14.3	2.9	2.6	2.6	3.3	3.6
∞	3.7	2.8	2.6	2.6	3.3	3.6

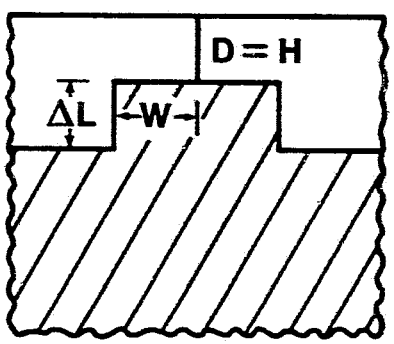

Figure 14: Magnitude and position of postseismic strain rate minimum for varying lithosphere model.

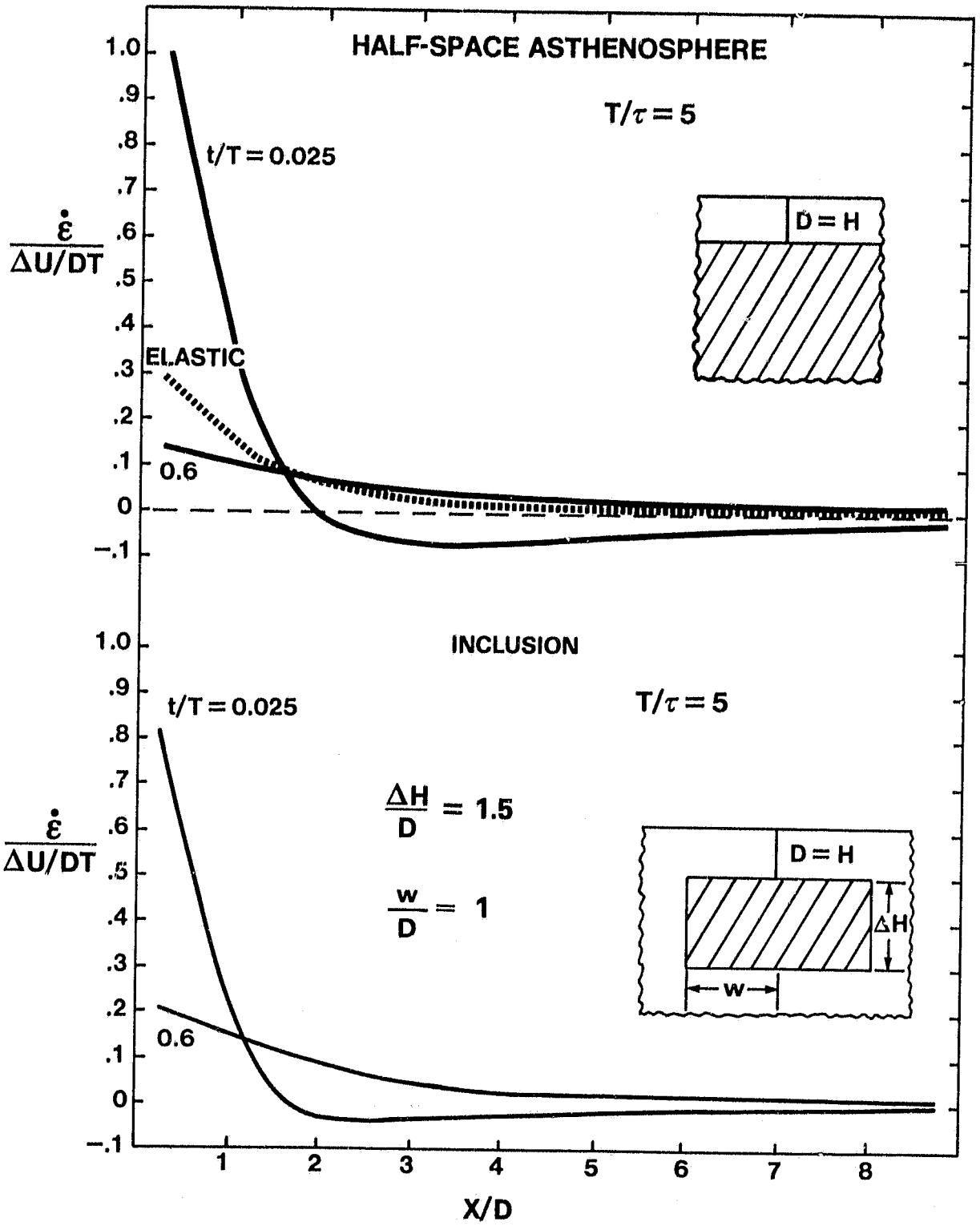

Figure 15: Strain rate versus distance from the fault at various times for the half-space asthenosphere and inclusion models.

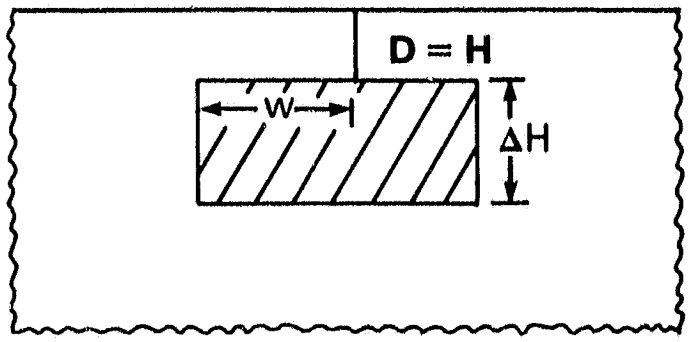

$H/D=1; T/\tau=5$

$$\frac{\dot{\varepsilon}}{\Delta U/DT}$$

$X/D = 0.275 \quad t/\tau = 0.025$

		w/D				
		0	.5	1	2	∞
ΔH/D	0	.30	.30	.30	.30	.30
	.5	.30	.63	.69	.72	.73
	1.0	.30	.68	.79	.85	.87
	1.5	.30	.69	.82	.91	.93
	∞	.30	.69	.84	.95	1.01

Figure 16: Near-field postseismic strain rate dependence on inclusion width and thickness.